NANOSYSTEMS: PHYSICS, CHEMISTRY, MATHEMATICS, 2021, 12 (4), P. 481–491

Study of magnetic and optical transitions in MFe_2O_4 (M=Co, Zn, Fe, Mn) with spinel structure

Nitika[1,*], Anu Rana[1], Vinod Kumar[2]

[1]Department of Physics, SRM University, Delhi NCR, Sonepat, 131029, India

[2]Department of Physics, NSUT, Dwarka, New Delhi, 110078, India

[*]nitika270593@gmail.com

DOI 10.17586/2220-8054-2021-12-4-481-491

Spinel ferrite (MFe_2O_4) nanoparticles were successfully synthesized by the coprecipitation method. X-ray diffraction technique was employed for structural analysis. Single-phase cubic spinel structure with an average crystallite size ranging from 5 – 20 nm was obtained for the prepared ferrites. The Fourier transform infrared spectra exhibits an absorption band at 550 cm^{-1}, which is attributed to metal-oxygen bond vibrations at tetrahedral sites. The thermogravimetric analysis revealed the instability of $MnFe_2O_4$ and Fe_3O_4 above 500 °C whereas $CoFe_2O_4$ is found to be the most stable ferrite. The hysteresis parameters demonstrate the superparamagnetic nature of the prepared nanoparticles with low coercivity except for $CoFe_2O_4$. The direct optical band gap energy derived from UV-visible spectra is calculated to be 2.82, 2.83, 2.81, and 2.44 eV for M=Co, Zn, Fe, and Mn respectively. The magnetic and optical properties show a strong dependence on cation site occupancy.

Keywords: Spinel ferrites, Fourier transform infrared spectroscopy, thermo-gravimetric analysis, hysteresis curve, optical properties.

Received: 10 May 2021

Revised: 27 July 2021

1. Introduction

Magnetic nanocrystalline bimetallic iron-based oxides are technologically important due to an excellent combination of structural, magnetic, and electrical properties. The transition metal oxides with formula MFe_2O_4, also termed as magnetic spinels, have attracted research interest in recent years attributable to their significant stability, ease of synthesis, high magnetization, low toxicity, small coercivity, less remanent magnetization, and high electrical resistance. The tunable magnetic and electrical properties of ferrites have turned the prime focus of researchers towards their potential use in biomedical and electronic applications [1–11]. The unique physicochemical properties are dependent on the structure of the crystal. The occupancy of metal cations on both sites is governed by electrostatic, elastic, and crystal field stabilization energy. Following the cation distribution, ferrites can be classified into normal, inverse, and mixed spinel. In normal spinel, the divalent cations occupy tetrahedral sites (A-sites), whereas the trivalent cations occupy octahedral sites (B-sites). On the contrary, in inverse spinel structure, divalent cations occupy B-sites, while trivalent cations occupy the A-sites. In mixed spinels, the site occupancy is intermediate to that of normal and inverse spinel structure [12–15]. Among ferrites, $CoFe_2O_4$, $ZnFe_2O_4$, Fe_3O_4, and $MnFe_2O_4$ nanoparticles have drawn appreciable attention due to their wide application range taking into consideration their magnificent properties. $CoFe_2O_4$ and Fe_3O_4 possess inverse spinel structures; $ZnFe_2O_4$ forms normal spinel ferrite, whereas $MnFe_2O_4$ represents mixed spinel ferrite with 80% predominantly inverse structure. Although significant research has been done which reports the physicochemical properties of all the above ferrites, a systematic and thorough investigation is imperative to study and compare the properties of transition metal nano-ferrites [16–22].

Naseri et al. [20] reviewed $ZnFe_2O_4$, $MnFe_2O_4$, and $CoFe_2O_4$ nanoparticles prepared by the thermal treatment method. The average particle size of prepared ferrites ranged from 15 nm to 21 nm with very low saturation magnetization (2 – 5 emu/g). The saturation magnetization values reported are not sufficient for their use in electronic devices and are not in agreement with previous reports [23–28]. Kolhatkar et al. [29] presented a review of magnetic nanoparticles focusing on magnetic properties. Pandervand et al. [30] studied XFe_2O_4 (X=Mn, Fe, Ni, Co, and Zn) nanoparticles prepared by coprecipitation and hydrothermal methods. The average particle size varied from 21 – 30 nm. The paper lacks any detailed discussion of magnetic behavior and its relation to the structure. Banerjee et al. [31] synthesized polyethylene glycol (PEG) coated transition metal ferrites and compared the observed properties. PEG coating increases saturation magnetization but is undesirable due to its nonbiodegradability and holds several drawbacks in the biomedical field [32, 33]. Moreover, insufficient literature exists highlighting the comparative study of optical and thermal properties. The properties of ferrites at the nanoscale are not well defined due to their dynamic behavior. Replication of experimental study is required to observe the patterns and trends in the behavior of the material and to conclude the findings based on sufficient evidence.

Therefore, in the present work, we investigate the properties of four different magnetic nanoparticles with varying spinel structures synthesized by the co-precipitation technique, which is a simple and cost-effective method with an eco-friendly route. The structural, magnetic, optical, and thermal properties of the obtained ferrites are studied and compared for a better understanding of structure-property relation from a specific application based-perspective.

2. Materials and methods

2.1. Synthesis method

Cobalt ferrite, zinc ferrite, ferrous ferrite, and manganese ferrite nanoparticles were prepared using the co-precipitation technique. Analytical grade chemical reagents used for preparation were $FeSO_4 \cdot 7H_2O$, $Fe(NO_3)_3 \cdot 9H_2O$, $Zn(NO_3)_2 \cdot 6H_2O$ $MnCl_2 \cdot 4H_2O$, and $CoCl_2 \cdot 6H_2O$. Separate homogeneous aqueous solutions of two precursors including $Fe(NO_3)_3 \cdot 9H_2O$ were prepared in distilled water with continuous stirring. The solutions were mixed, keeping the resultant solution at 70 °C. Surfactant (oleic acid) was added to avoid agglomeration. After 30 min, aqueous NH_3 was added drop-wise with uninterrupted stirring to attain pH 11. The precipitates so formed were finally dried at 80 °C on a hot plate followed by crushing using agate mortar. Further, the prepared samples were annealed at 300 °C for 2 hrs to improve their crystalline properties. The physicochemical properties of obtained samples were studied using various characterization techniques.

2.2. Characterization tools

Powder X-ray diffraction measurements were performed in the 2θ range of 20 – 70 ° with a scan rate of 5 °/min using Cu-Kα radiation ($\lambda = 1.5406$ Å). Thermogravimetric analysis (TGA) was carried out to study mass loss at a heating rate of 10 °C/min by varying temperature from room temperature to 800 °C in an aerobic atmosphere. FTIR spectra were recorded using a Perkin Elmer Frontier FTIR spectrophotometer in the range of 4000 – 450 cm^{-1}. Magnetic measurements were recorded using a Vibrating sample magnetometer (Lakeshore model 7400) at room temperature within the range of ± 1.5 T. The absorption spectra are obtained using an Ultraviolet spectrophotometer by Perkin Elmer (LAMBDA 950) in the range 200 – 1600 nm.

3. Results and Discussion

3.1. Structural analysis

Figure 1 shows the XRD pattern of $CoFe_2O_4$ (CNP), $ZnFe_2O_4$ (ZNP), Fe_3O_4 (FNP) and $MnFe_2O_4$ (MNP). The formation of a single-phase spinel cubic structure with an Fd3m space group for all the samples is confirmed by the diffraction peaks (JCPDS #22-1086, #89-1010, #19-0629, #73-1964). The average crystallite size is calculated using the most intense peak belonging to the (311) plane by employing the Scherrer formula (1).

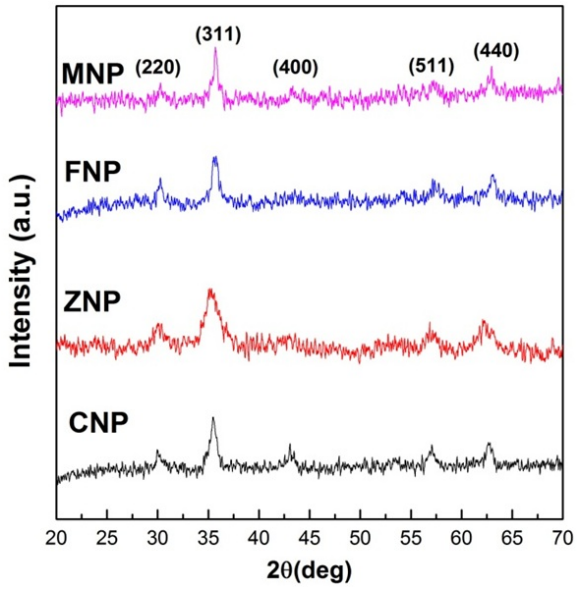

FIG. 1. XRD pattern of $CoFe_2O_4$ (CNP), $ZnFe_2O_4$ (ZNP), Fe_3O_4 (FNP), $MnFe_2O_4$ (MNP) nanoparticles

TABLE 1. Average crystallite size, lattice parameter, X-ray density, specific surface area, micro-strain and dislocation density for CNP, ZNP, FNP, and MNP

Sample	Average crystallite size D (nm)	Lattice Parameter a(Å)	X-ray Density ρ_x (g/cc)	Specific surface area S (m^2/g)	Micro-strain ε	Dislocation Density ρ_D (10^{15} m^{-2})
CNP	11.35	8.381	5.29	99.85	0.003	4.82
ZNP	5.89	8.411	5.38	189.28	0.006	17.81
FNP	12.54	8.337	5.31	90.14	0.003	3.97
MNP	19.86	8.334	5.29	57.08	0.002	1.58

TABLE 2. Interionic distances and hopping lengths at A and B sites for CNP, ZNP, FNP and MNP

Sample	d_{AL}(Å)	d_{BL}(Å)	d_{AE}(Å)	d_{BE}(Å)	d_{BEU}(Å)	L_A(Å)	L_B(Å)
CNP	1.8871	2.0542	3.0817	2.8446	2.9643	3.6291	2.9631
ZNP	1.8939	2.0616	3.0927	2.8548	2.9749	3.6421	2.9737
FNP	1.8772	2.0434	3.0655	2.8297	2.9488	3.6100	2.9476
MNP	1.8765	2.0427	3.0644	2.8287	2.9477	3.6087	2.9465

$$D = \frac{K\lambda}{\beta \cos\theta}, \tag{1}$$

where D is the average crystallite size, K is Scherrer constant (0.9 for spherical crystallites with Cubic symmetry), λ is X-ray wavelength (1.5406 Å), β is FWHM of XRD peak in radians, θ is the diffraction angle. The lattice parameter (a) is calculated using (2) [34]:

$$a = d\sqrt{h^2 + k^2 + l^2}, \tag{2}$$

where d is interplanar spacing and h, k, l is the Miller indices. All the elementary information like X-ray density ρ_x, specific surface area (S), micro-strain (ε), and dislocation density ρ_D can be retrieved from the XRD pattern using the below-mentioned formulas (3-6):

$$\rho_x = \frac{ZM}{Na^3}, \tag{3}$$

$$S = \frac{6}{\rho_x D}, \tag{4}$$

$$\varepsilon = \frac{\beta \cos\theta}{4}, \tag{5}$$

$$\rho_D = \frac{15\varepsilon}{aD}, \tag{6}$$

where Z, M, N, β, and θ denote the number of atoms per unit cell, molecular weight, Avogadro's number, full width at half maximum, and diffraction angle respectively. The values obtained are tabulated in Table 1. Considering the preferred spinel structure, site occupancy, crystal field stabilization energy, and coordination number (CN), the ionic radii of all the cations can be chosen from the database of ionic radii [35]. The estimated ionic radii are 0.785 Å for Fe^{3+} ions at B sites, 0.63 Å for Fe^{3+} ions at A sites, 0.88 Å for Co^{2+} ions (as it occupies B sites with CN 6 being in the high spin state), 0.74 Å for Zn^{2+} ions (as it occupies A sites with CN 4 being in the high spin state), 0.92 Å for Fe^{2+} ions (as it occupies B sites with CN 6 being in the high spin state) and 0.80 Å for Mn^{2+} ions at A sites and 0.97 Å for Mn^{2+} ions at B sites [36–38]. The hopping lengths (L_A and L_B), interionic distances (i.e., M–O bond length at A site (d_{AL}), M–O bond length at B site (d_{BL}), tetrahedral and octahedral shared edge length (d_{AE} and d_{BE}), and unshared octahedral edge length (d_{BEU}) are calculated using the relations 7 – 13 [39–42].

$$L_A = \sqrt{3}a/4, \tag{7}$$

$$L_B = \sqrt{2}a/4, \tag{8}$$

$$d_{AL} = a\sqrt{3}(u - 0.25), \tag{9}$$

$$d_{BL} = a\sqrt{(3u^2 - \frac{11u}{4} + \frac{43}{64})}, \tag{10}$$

$$d_{AE} = a\sqrt{2}\,(2u - 0.5)\,, \tag{11}$$

$$d_{BE} = a\sqrt{2}(1 - 2u), \tag{12}$$

$$d_{BEU} = a\sqrt{4u^2 - 3u + \frac{11}{16}}, \tag{13}$$

where u is the oxygen positional parameter. The calculated values are listed in Table 2. From the variation observed in the interionic distances and hopping lengths, it can be inferred that the lattice parameter is strongly influenced by the distances between cations and anions. In the present study, all the cases possess different spinel structures; hence the lattice parameter cannot be compared. Although a cation distribution can be proposed by correlating the lattice parameter and the magnetic measurements which depend on the cations site occupancy. Former studies reveal that effective magnetism is observed in inverse and mixed spinel structures where A–B interactions are dominant. The average crystallite size, lattice parameter, and magnetic moments of the cations determine the magnetic properties of spinel ferrites [1].

3.2. Thermogravimetric analysis

Mass loss of prepared samples (TGA) and the first derivative of TGA (DTG) as a function of temperature are shown in Fig. 2. The thermal decomposition of CNP and ZNP takes place in two stages, whereas that of FNP and MNP takes place in three stages. The initial weight loss up to 250 °C is due to the loss of adsorbed water. This weight loss is approximately 6%, 2%, 6.6%, and 12% for CNP, ZNP, FNP, and MNP respectively which indicates surface water adsorption is highest for MNP and least for ZNP. The second mass loss up to 550 °C is due to the evaporation of surfactant used in the synthesis process. The boiling point of oleic acid used in the synthesis is 360 °C. Approximately 40%, 57%, 35%, and 34.8% mass loss is observed in this range corresponding to CNP, ZNP, FNP, and MNP respectively. This major loss indicates that nanoparticles prepared with the coprecipitation technique contained a large amount of organic compound. It can be inferred in the synthesis process, organic content increased in the order MNP<FNP<CNP<ZNP with a corresponding decrease in particle size. This phenomenon can be attributed to the increase in specific surface area in the order MNP<FNP<CNP<ZNP. The same trend has been reported and explained previously [43–45]. The third mass loss of 4% at 600 °C for FNP is due to the formation of secondary phases (α-Fe_2O_3 and γ-Fe_2O_3). The formation of these phases at higher temperatures is favorable due to its thermal stability above 570 °C [46]. A similar minor mass loss of 0.5% above 700 °C for MNP indicates the partial decomposition of $MnFe_2O_4$ to α-Mn_2O_3 and α-Fe_2O_3 [47, 48]. This signifies an increase in impurity phases in MNP at a higher temperature. As the temperature reaches 800 °C, the remaining mass% values of the samples were 51.6%, 42.2%, 52.3%, and 49.1% for CNP, ZNP, FNP, and MNP respectively. The analysis of all the TGA/DTG curves suggests thermal stability in the order CNP>ZNP>MNP>FNP.

3.3. Fourier transform infrared spectroscopy analysis

Figure 3 shows FTIR spectra of CNP, ZNP, FNP, and MNP respectively. The absorption bands between 3600 – 3300, 1700 – 1500 and 1000 – 1200 cm^{-1} correspond to stretching and bending of H_2O molecules [49]. Low-intensity peaks are observed in the above-mentioned regions corresponding to ZNP indicating less surface water adsorption by the particles. Although the peaks for ZNP belonging to range 2800 – 2900 cm^{-1} are more intense, indicating the presence of organic groups more than others. Oleic acid inhibits grain growth by binding the surface molecules which in turn induces strain [50]. The same has been proved in XRD and TGA analysis for ZNP. The peaks belonging to region 1300 – 1500 cm^{-1} are attributed to the stretching and bending of the COO- group [51]. The presence of absorption band at frequency $\sim$550 cm^{-1} for all the samples is attributed to the intrinsic vibrations of the M–O bonds (M=Co, Zn, Fe, Mn) at tetrahedral sites which is the characteristic feature confirming the formation of spinel ferrite structures [52]. It is also observed that wavenumber corresponding to tetrahedral vibrations increases in the order FNP<ZNP<MNP<CNP respectively. The same trend has been observed in various reports [53]. This phenomenon particularly depends on the cation distribution, cation mass, and the ionic radii of the divalent cations.

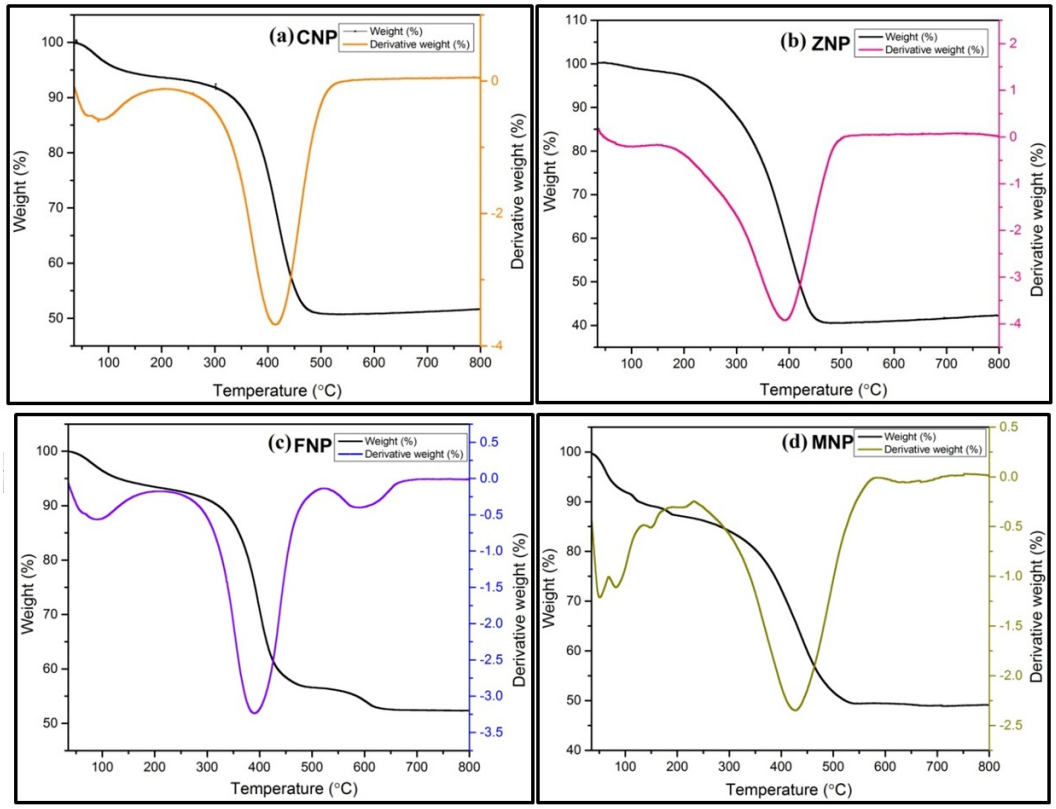

FIG. 2. TGA-DTG curve for (a) CNP (b) ZNP (c) FNP (d) MNP

TABLE 3. Magnetic parameters for CNP, ZNP, FNP, and MNP

Samples	M_S(emu/g)	H_C(Oe)	M_R(emu/g)	R	K(erg/Oe)	$\eta_B(\mu_B)$
CNP	35.55	595.34	8.98	0.253	21593.22	1.493
ZNP	15.29	51.43	0.41	0.027	802.34	0.660
FNP	26.04	15.62	0.44	0.017	415.10	1.079
MNP	14.94	97.88	1.65	0.111	1492.59	0.617

3.4. Magnetic properties

Fig. 4 shows the magnetization curves for CNP, ZNP, FNP, and MNP recorded at room temperature. The values of saturation magnetization (M_S), coercivity (H_C), retentivity (M_R), squareness ratio (R), magnetic anisotropy constant (K), and magnetic moment (η_B) are tabulated in Table 3 [54]. The relation between magnetic anisotropy constant, squareness ratio, and magnetic moment is given below:

$$K = \frac{H_C M_S}{0.98}, \tag{14}$$

$$R = \frac{M_R}{M_S}, \tag{15}$$

$$\eta_B = \frac{(M \times M_S)}{5585}. \tag{16}$$

The variation of M_S follows the order CNP>FNP>ZNP>MNP. However, a very small difference exists between M_S of MNP and ZNP. Saturation magnetization is mainly governed by cation distribution and average crystallite size. Magnetic moments corresponding to different cations belonging to high spin state follows the order of Mn^{2+}=Fe^{3+}(5.92 μ_B)>Fe^{2+}(4.90 μ_B)>Co^{2+}(3.87 μ_B)>Zn^{2+}(0 μ_B) [55,56]. The variation of M_S can be explained

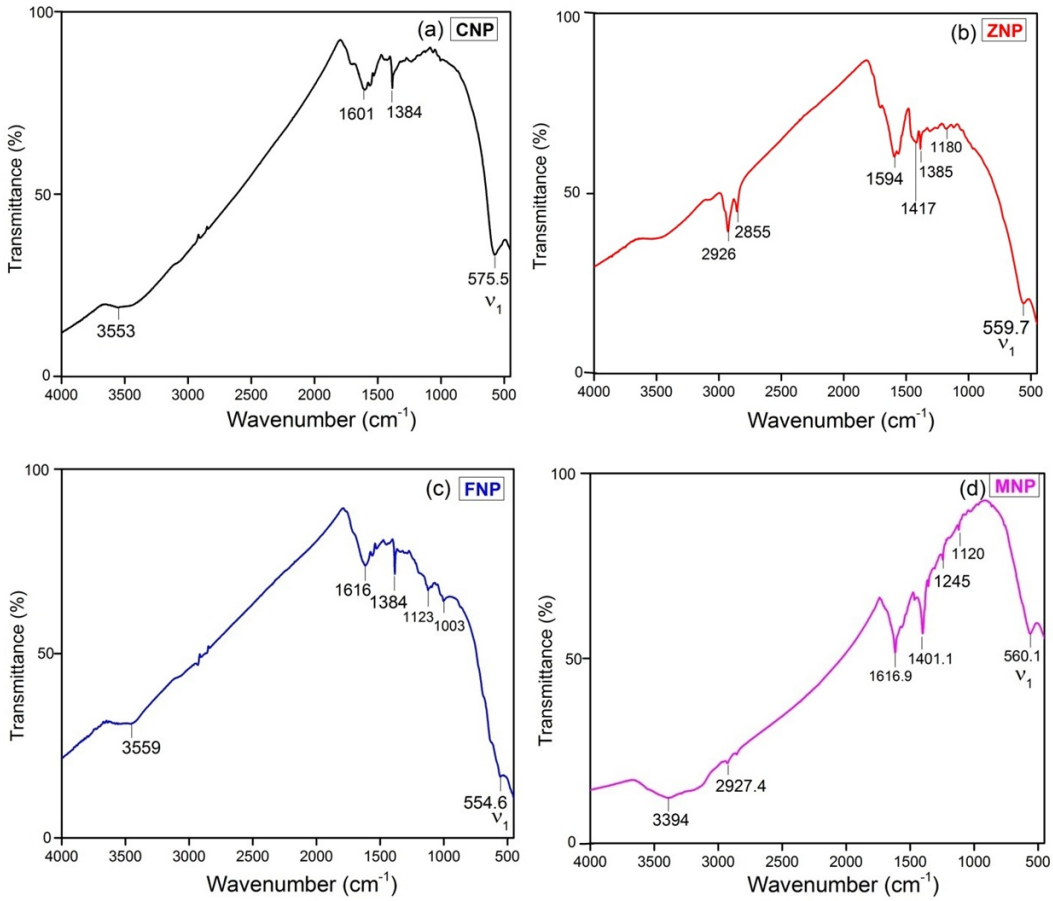

FIG. 3. FTIR Spectra for (a) CNP (b) ZNP (c) FNP (d) MNP

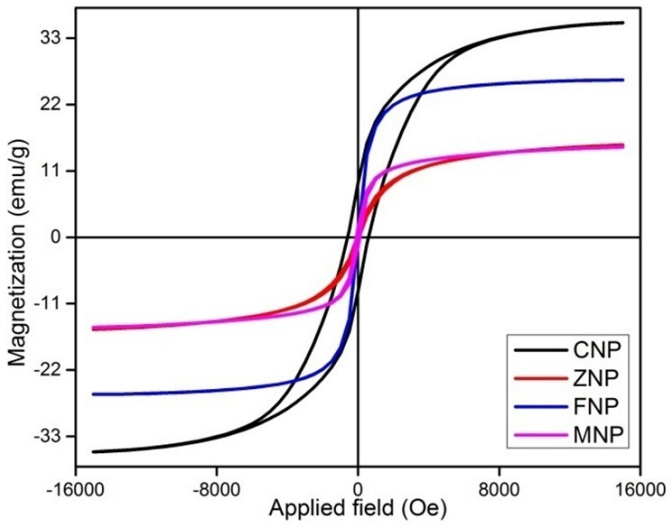

FIG. 4. Magnetic hysteresis curves for CNP, ZNP, FNP, and MNP

efficiently by taking into consideration their respective spinel structure and net magnetic moment. The net magnetization per formula unit is calculated using Neel's model where n_{net} is the difference between net magnetization at B-sites and net magnetization at A-sites [57]. CNP belongs to the inverse spinel structure, with a majority of Co^{2+} ions and Fe^{3+} ions occupying B-sites. This increases the net magnetic moment which is clear from the data in the table. FNP also belongs to inverse spinel structure, due to which net magnetization of B-sites is greater than that of A-sites, thereby yielding a high magnetic moment. A slight variation of the net magnetic moment for both the ferrites is due to the inversion degree. The fraction of Co^{2+} ions occupying B-sites in CNP is greater than that of Fe^{2+} ions in FNP. ZNP belongs to a normal spinel structure in which a maximum of non-magnetic Zn^{2+} ions occupy the A-sites. A small magnetic moment of 0.6 μ_B agrees well with previous reports, which is correlated with a low fraction of Fe^{3+} ions in A-sites [12]. MNP belongs to a mixed spinel structure in which Mn^{2+} ions get distributed between both sites. Moreover, the magnetic moments of Mn^{2+} and Fe^{3+} are equal, resulting in very small magnetic moments. Small values of coercivity and retentivity for all the prepared ferrites except CNP indicate superparamagnetic nature. However, CNP exhibits ferromagnetic behavior. CNP possessed the highest coercivity with a highly anisotropic structure. The values of MR, HC, and K follow the same variation as M_S. The squareness ratio termed as Stoner–Wohlfarth value is less than 0.5 signifying uniaxial anisotropy influenced by lattice strain [58].

3.5. Optical properties

Figure 5 shows the absorption spectra of CNP, ZNP, FNP, and MNP demonstrating the absorption in the visible and near-infrared region. The absorption band of MNP shows a shoulder-like structure attributed to the absorption taking place due to surface states [59].

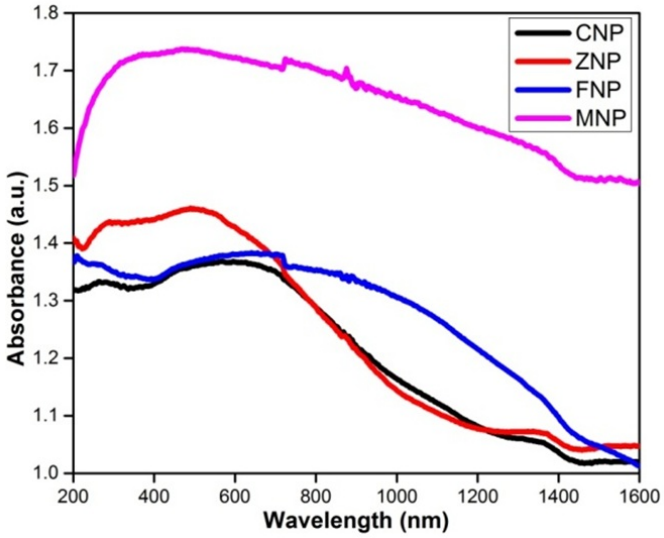

FIG. 5. Absorption spectra for CNP, ZNP, FNP, and MNP

The absorption spectrum is obtained due to the transition of the electrons from the valence band of O-2p to the conduction band of Fe-3d. The absorption in the visible region is highest in the case of MNP whereas it is least in the case of CNP. The optical band gap for direct transitions can be calculated using the Tauc plots by employing (17) (Fig. 6) [60]:

$$\alpha h\nu = A\sqrt{(h\nu - E_g)}, \tag{17}$$

where α is the absorption coefficient, $h\nu$ is the energy of the photon, E_g is the optical band gap and A is the proportionality constant.

The obtained values of optical band gaps are tabulated in Table 4. The optical bandgaps of prepared spinel ferrites varied from 2.44 – 2.83 eV. The tuning of bandgap signifies the potential of bandgap engineering in spinel ferrites. The variation observed in the optical band gap is explained by correlating it with average crystallite size. A decrease in average crystallite size increases the binding energy of valence electrons and parent atoms, which increases the bandgap energy [61]. The trend verifies Brass's effective mass model. The optical band gap is also influenced by the site occupancy of transition metal cation [56]. The spinel ferrites possess good absorption properties in the visible region which makes them suitable for optoelectronic devices. The study of optical properties is quite useful for photocatalytic reactions.

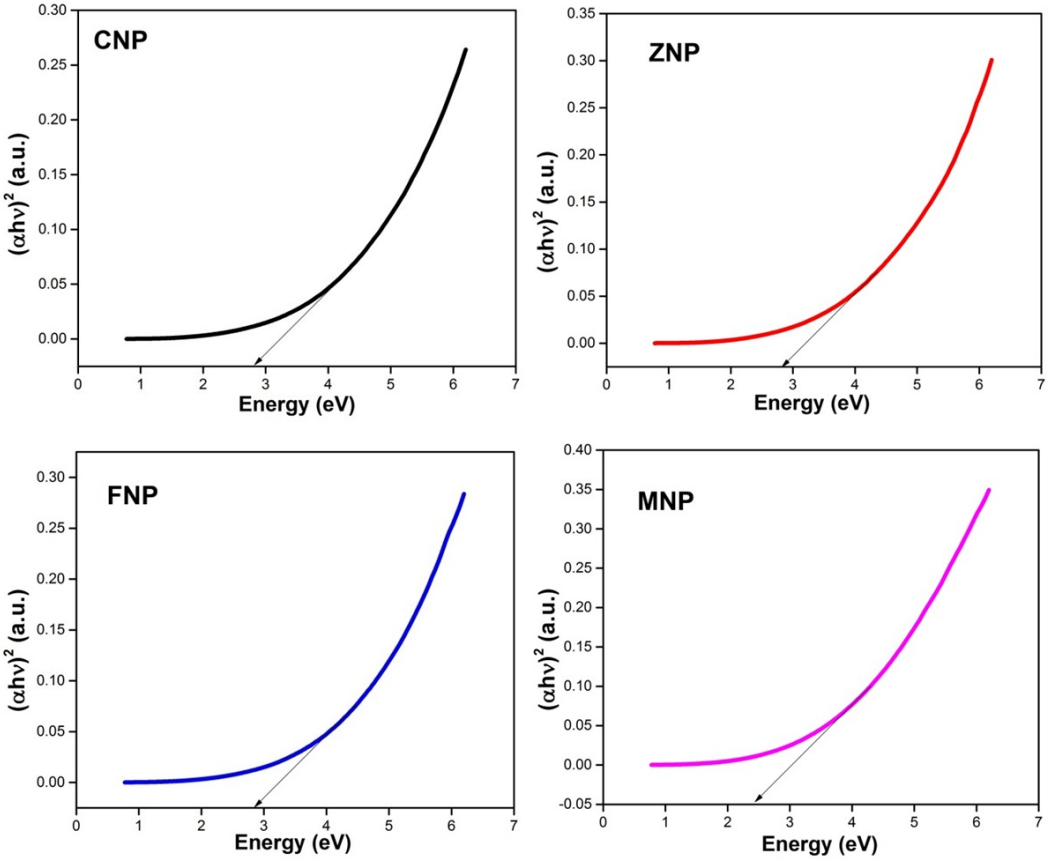

FIG. 6. Plot of $(\alpha h\nu)^2$ as a function of photon energy (eV) for CNP, ZNP, FNP, and MNP

TABLE 4. Optical bandgaps for CNP, ZNP, FNP, and MNP

Sample	Optical band gap (eV)	Refractive index (n)	Real dielectric constant (ε')	Imaginary dielectric constant (ε'')
CNP	2.82	2.40	3.97	6.47
ZNP	2.83	2.40	3.66	6.96
FNP	2.81	2.41	3.96	6.52
MNP	2.44	2.53	3.41	8.80

The Ravindra empirical relation can be employed to calculate optical parameters such as the refractive index (n), real and imaginary part of dielectric constant (ε' and ε'') [62, 63]. The values obtained using the below relations (18–21) are shown in Table 4:

$$n = A + (B \times E_g), \tag{18}$$

$$k = \frac{\alpha\lambda}{4\pi}, \tag{19}$$

$$\varepsilon' = n^2 - k^2, \tag{20}$$

$$\varepsilon'' = 2 \times n \times k, \tag{21}$$

where $A = 4.05$ eV^{-1}, $B = -0.62$ eV^{-1}, k is the extinction coefficient, α is the absorption coefficient and λ is the wavelength calculated from bandgap energy. The high value of the refractive index for MNP makes it suitable for antireflection coatings. It can be inferred that optical conductivity strongly depends on the absorption coefficient [64].

4. Conclusion

The physicochemical properties of spinel ferrites entirely depend on the crystal structure and cation distribution. In the present study, four different spinel ferrites belonging to normal, inverse, and mixed spinel structure were successfully synthesized using the chemical co-precipitation technique. XRD confirmed the formation of single-phase cubic spinel structures with average crystallite sizes of 11 nm, 6 nm, 13 nm, and 20 nm for $CoFe_2O_4$, $ZnFe_2O_4$, Fe_3O_4, and $MnFe_2O_4$ respectively. The lattice parameter ranged from 8.334 – 8.411 Å. The specific surface area was highest for $ZnFe_2O_4$ and least for $MnFe_2O_4$ nanoparticles. TGA/DTG curves illustrated thermal stability in the order $CoFe_2O_4$ >$ZnFe_2O_4$ >$MnFe_2O_4$ >Fe_3O_4. The fundamental peak attributed to tetrahedral M–O bond vibrations was obtained around 550 cm^{-1} confirming the formation of spinel ferrites. All the ferrites exhibited superparamagnetic behavior except $CoFe_2O_4$. $CoFe_2O_4$ showed ferromagnetic behavior with high magnetic coercivity and anisotropy. The saturation magnetization and coercivity ranged from 14.94 emu/g to 35.55 emu/g and 15.62 – 595.34 Oe respectively. A strong dependence of optical properties on average crystallite size was observed. $MnFe_2O_4$ has the highest refractive index and imaginary dielectric constant but the least real dielectric constant. Optical conductivity depends on the absorption coefficient. The study of optical and magnetic properties is useful in determining the applications of the prepared ferrites in electrical and magnetic devices.

Acknowledgement

The author(s) received no financial support for the research, authorship, and/or publication of this article.

References

[1] Galvão W.S., Neto D., Freire R.M., Fechine P.B. Super-paramagnetic nanoparticles with spinel structure: a review of synthesis and biomedical applications. *In solid state phenomena*, 2016, **241**, P. 139–176.

[2] Valenzuela R. *Novel applications of ferrites*. Physics Research International, 2012.

[3] Tatarchuk T., Bououdina M., Vijaya J.J., Kennedy L.J. Spinel ferrite nanoparticles: synthesis, crystal structure, properties, and perspective applications. *In International Conference on Nanotechnology and Nanomaterials*, 2016, August, P. 305–325.

[4] Kombaiah K., Vijaya J.J., Kennedy L.J., Bououdina M. Optical, magnetic and structural properties of $ZnFe_2O_4$ nanoparticles synthesized by conventional and microwave assisted combustion method: a comparative investigation. *Optik*, 2017, **129**, P. 57–68.

[5] Brabers V.A.M. Progress in spinel ferrite research. *Handbook of magnetic materials*, 1995, **8**, P. 189–324.

[6] Mathew D.S., Juang R.S. An overview of the structure and magnetism of spinel ferrite nanoparticles and their synthesis in microemulsions. Chemical engineering journal, 2007, **129**(1-3), P. 51–65.

[7] Amiri M., Salavati-Niasari M., Akbari A. Magnetic nanocarriers: evolution of spinel ferrites for medical applications. *Advances in Colloid and Interface Science*, 2019, **265**, P. 29–44.

[8] Bao N., Shen L., Wang Y., Padhan P., Gupta A. A facile thermolysis route to monodisperse ferrite nanocrystals. *Journal of the American Chemical Society*, 2007, 129(41), P. 12374–12375.

[9] Srinivas C., Kumar E.R., Tirupanyam B.V., Meena S.S., Bhatt P., Prajapat C.L., Sastry D.L. Study of magnetic behavior in co-precipitated Ni–Zn ferrite nanoparticles and their potential use for gas sensor applications. *Journal of Magnetism and Magnetic Materials*, 2020, **502**, P. 166534.

[10] Kannapiran N., Muthusamy A., Renganathan B., Ganesan A.R., Meena S.S. Magnetic, electrical and gas sensing properties of poly (o-phenylenediamine)/$MnCoFe_2O_4$ nanocomposites. *Applied Physics A*, 2020, **126**(12), P. 1–13.

[11] Deepty M.Ch.S., Ramesh P.N., Mohan N.K., Singh M.S., Prajapat C.L., Sastry D.L. Evaluation of structural and dielectric properties of Mn^{2+}-substituted Zn-spinel ferrite nanoparticles for gas sensor applications. *Sensors and Actuators B: Chemical*, 2020, **316**, P. 128127.

[12] Andersen H.L., Saura-Múzquiz M., Granados-Miralles C., Canévet E., Lock N., Christensen M. Crystalline and magnetic structure–property relationship in spinel ferrite nanoparticles. *Nanoscale*, 2018, **10**(31), P. 14902–14914.

[13] Chand P., Vaish S., Kumar P. Structural, optical and dielectric properties of transition metal (MFe_2O_4; M= Co, Ni and Zn) nanoferrites. *Physica B: Condensed Matter*, 2017, **524**, P. 53–63.

[14] Bid S., Pradhan S.K. Preparation of zinc ferrite by high-energy ball-milling and microstructure characterization by Rietveld's analysis. *Materials Chemistry and Physics*, 2003, **82**(1), P. 27–37.

[15] Rahman S., Nadeem K., Anis-ur-Rehman M., Mumtaz M., Naeem S., Letofsky-Papst I. Structural and magnetic properties of ZnMg-ferrite nanoparticles prepared using the co-precipitation method. *Ceramics International*, 2013. **39**(5), P. 5235–5239.

[16] Maaz K., Mumtaz A., Hasanain S.K., Ceylan A. Synthesis and magnetic properties of cobalt ferrite ($CoFe_2O_4$) nanoparticles prepared by wet chemical route. *Journal of magnetism and magnetic materials*, 2007, **308**(2), P. 289–295.

[17] Houshiar M., Zebhi F., Razi Z.J., Alidoust A., Askari Z. Synthesis of cobalt ferrite ($CoFe_2O_4$) nanoparticles using combustion, coprecipitation, and precipitation methods: A comparison study of size, structural, and magnetic properties. Journal of Magnetism and Magnetic Materials, 2014, **371**, P. 43–48.

[18] Vinosha P.A., Mely L.A., Jeronsia J.E., Krishnan S., Das S.J. Synthesis and properties of spinel $ZnFe_2O_4$ nanoparticles by facile co-precipitation route. *Optik*, 2017, **134**, P. 99–108.

[19] Zipare K., Dhumal J., Bandgar S., Mathe V., Shahane G. Superparamagnetic manganese ferrite nanoparticles: synthesis and magnetic properties. *Journal of Nanoscience and Nanoengineering*, 2015, **1**(3), P. 178–182.

[20] Liu C., Zou B., Rondinone A.J., Zhang Z.J. Reverse micelle synthesis and characterization of superparamagnetic $MnFe_2O_4$ spinel ferrite nanocrystallites. The Journal of Physical Chemistry B, 2000, **104**(6), P. 1141–1145.

[21] Gholizadeh A. A comparative study of physical properties in Fe_3O_4 nanoparticles prepared by coprecipitation and citrate methods. Journal of the American Ceramic Society, 2017, **100**(8), P. 3577–3588.

[22] Kandpal N.D., Sah N., Loshali R., Joshi R., Prasad J. Co-precipitation method of synthesis and characterization of iron oxide nanoparticles, 2014.

[23] Goodarz Naseri M., Saion E.B., Kamali A. An overview on nanocrystalline $ZnFe_2O_4$, $MnFe_2O_4$, and $CoFe_2O_4$ synthesized by a thermal treatment method. International Scholarly Research Notices, 2012.

[24] Naik S.R., Salker A.V., Yusuf S.M., Meena S.S. Influence of Co^{2+} distribution and spin–orbit coupling on the resultant magnetic properties of spinel cobalt ferrite nanocrystals. *Journal of alloys and compounds*, 2013, **566**, P. 54–61.

[25] Vasundhara K., Achary S.N., Deshpande S.K., Babu P.D., Meena S.S., Tyagi A.K. Size dependent magnetic and dielectric properties of nano $CoFe_2O_4$ prepared by a salt assisted gel-combustion method. *Journal of Applied Physics*, 2013, **113**(19), P. 194101.

[26] Patange S.M., Desai S.S., Meena S.S., Yusuf S.M., Shirsath S.E. Random site occupancy induced disordered Néel-type collinear spin alignment in heterovalent Zn^{2+}–Ti^{4+} ion substituted $CoFe_2O_4$. *RSC advances*, 2015, **5**(111), P. 91482–91492.

[27] Yadav S.P., Shinde S.S., Bhatt P., Meena S.S., Rajpure K.Y. Distribution of cations in Co^{1-} xMnxFe2O4 using XRD, magnetization and Mössbauer spectroscopy. *Journal of Alloys and Compounds*, 2015, **646**, P. 550–556.

[28] Hashim M., Shirsath S.E., Meena S.S., Mane M.L., Kumar S., Bhatt P., Şentürk E. Manganese ferrite prepared using reverse micelle process: Structural and magnetic properties characterization. *Journal of Alloys and Compounds*, 2015, **642**, P. 70–77.

[29] Kolhatkar A.G., Jamison A.C., Litvinov D., Willson R.C., Lee T.R. Tuning the magnetic properties of nanoparticles. International journal of molecular sciences, 2013, **14**(8), P. 15977–16009.

[30] Padervand M., Vossoughi M., Yousefi H., Salari H., Gholami M.R. An experimental and theoretical study on the structure and photoactivity of XFe2O4 (X= Mn, Fe, Ni, Co, and Zn) structures. *Russian Journal of Physical Chemistry A*, 2014, **88**(13), P. 2451–2461.

[31] Banerjee A., Blasiak B., Pasquier E., Tomanek B., Trudel S. Synthesis, characterization, and evaluation of PEGylated first-row transition metal ferrite nanoparticles as T 2 contrast agents for high-field MRI. *RSC advances*, 2017, **7**(61), P. 38125–38134.

[32] Sebak A.A. Limitations of PEGylated nanocarriers: unfavourable physicochemical properties, biodistribution patterns and cellular and subcellular fates. *Int. J. Pharm*, 2018, **10**, P. 6–12.

[33] Patsula V., Horák D., Kučka J., Macková H., Lobaz V., Francová P., Šefc L. Synthesis and modification of uniform PEG-neridronate-modified magnetic nanoparticles determines prolonged blood circulation and biodistribution in a mouse preclinical model. Scientific reports, 2019, **9**(1), P. 1–12.

[34] Cullity B.D. *Elements of X-ray Diffraction*. Addison-Wesley Publishing, 1956.

[35] Shannon R.D. Revised effective ionic radii and systematic studies of interatomic distances in halides and chalcogenides. *Acta crystallographica section A: crystal physics, diffraction, theoretical and general crystallography*, 1976, **32**(5), P. 751–767.

[36] Grimes N.W., Thompson P., Kay H.F. New symmetry and structure for spinel. Proceedings of the Royal Society of London. A. Mathematical and Physical Sciences, 1983, **386**(1791), P. 333–345.

[37] Hwang L., Heuer A.H., Mitchell T.E. On the space group of MgAl2O4 spinel. *Philosophical Magazine*, 1973, **28**(1), P. 241–243.

[38] Burdett J.K., Price G.D., Price S.L. Role of the crystal-field theory in determining the structures of spinels. *Journal of the American Chemical Society*, 1982, **104**(1), P. 92–95.

[39] Arean C.O., Diaz E.G., Gonzalez J.R., Garcia M.V. Crystal chemistry of cadmium-zinc ferrites. *Journal of Solid State Chemistry*, 1988, **77**(2), P. 275–280.

[40] Gillot B., Jemmali F. Dependence of electrical properties in iron—cobalt, iron—zinc ferrites near stoichiometry on firing temperature and atmosphere. *Physica status solidi (a)*, 1983, **76**(2), P. 601–608.

[41] Pathan A.T., Mathad S.N., Shaikh A.M. Infrared spectral studies of nanostructured Co^{2+}-substituted Li-Ni-Zn ferrites. *International Journal of Self-Propagating High-Temperature Synthesis*, 2014, **23**(2), P. 112–117.

[42] Mohammed K.A., Al-Rawas A.D., Gismelseed A.M., Sellai A., Widatallah H.M., Yousif A., Shongwe, M. Infrared and structural studies of Mg1–xZnxFe2O4 ferrites. *Physica B: Condensed Matter*, 2012, **407**(4), P. 795–804.

[43] Pereira C., Pereira A.M., Fernandes C., Rocha M., Mendes R., Fernández-García M.P., Freire C. Superparamagnetic MFe_2O_4 (M= Fe, Co, Mn) nanoparticles: tuning the particle size and magnetic properties through a novel one-step coprecipitation route. *Chemistry of Materials*, 2012, **24**(8), P. 1496–1504.

[44] Si S., Kotal A., Mandal T.K., Giri S., Nakamura H., Kohara T. Size-controlled synthesis of magnetite nanoparticles in the presence of polyelectrolytes. *Chemistry of Materials*, 2004, **16**(18), P. 3489–3496.

[45] Roca A.G., Marco J.F., Morales M.D.P., Serna C.J. Effect of nature and particle size on properties of uniform magnetite and maghemite nanoparticles. *The Journal of Physical Chemistry C*, 2007, **111**(50), P. 18577–18584.

[46] Mahdavi M., Ahmad M.B., Haron M.J., Namvar F., Nadi B., Rahman M.Z.A., Amin J. Synthesis, surface modification and characterisation of biocompatible magnetic iron oxide nanoparticles for biomedical applications. *Molecules*, 2013, **18**(7), P. 7533–7548.

[47] Aijun H., Juanjuan L., Mingquan Y., Yan L.I., Xinhua P. Preparation of nano-$MnFe_2O_4$ and its catalytic performance of thermal decomposition of ammonium perchlorate. *Chinese Journal of Chemical Engineering*, 2011, **19**(6), P. 1047–1051.

[48] Stoia M., Păcurariu C., Muntean E.C. Thermal stability of the solvothermal-synthesized $MnFe_2O_4$ nanopowder. *Journal of Thermal Analysis and Calorimetry*, 2017, **127**(1), P. 155–162.

[49] Umare S.S., Ningthoujam R.S., Sharma S.J., Shrivastava S., Kurian S., Gajbhiye N.S. Mössbauer and magnetic studies on nanocrystalline NiFe2O4 particles prepared by ethylene glycol route. *In ICAME*, 2007, P. 649–657.

[50] Limaye M.V., Singh S.B., Date S.K., Kothari D., Reddy V.R., Gupta A., Kulkarni S.K. High coercivity of oleic acid capped $CoFe_2O_4$ nanoparticles at room temperature. The Journal of Physical Chemistry B, 2009, **113**(27), P. 9070–9076.

[51] Nandiyanto A.B.D., Oktiani R., Ragadhita R. How to read and interpret FTIR spectroscope of organic material. *Indonesian Journal of Science and Technology*, 2019, **4**(1), P. 97–118.

[52] Pradeep A., Chandrasekaran G. FTIR study of Ni, Cu and Zn substituted nano-particles of MgFe2O4. *Materials Letters*, 2006, **60**(3), P. 371–374.

[53] Bera P., Lakshmi R.V., Prakash B.H., Tiwari K., Shukla A., Kundu A.K., Barshilia H.C. Solution combustion synthesis, characterization, magnetic, and dielectric properties of $CoFe_2O_4$ and Co0.5M0.5Fe2O4 (M= Mn, Ni, and Zn). *Physical Chemistry Chemical Physics*, 2020, **22**(35), P. 20087–20106.

[54] Nikmanesh H., Kameli P., Asgarian S.M., Karimi S., Moradi M., Kargar Z., Salamati H. Positron annihilation lifetime, cation distribution and magnetic features of Ni 1- x Zn x Fe 2- x Co x O 4 ferrite nanoparticles. *RSC Advances*, 2017, **7**(36), P. 22320–22328.

[55] Carter C.B., Norton M.G. Using Magnetic Fields and Storing Data. *Ceramic Materials: Science and Engineering*, 2007, P. 598–618.
[56] Szotek Z., Temmerman W. M., Ködderitzsch D., Svane A., Petit L., Winter H. Electronic structures of normal and inverse spinel ferrites from first principles. *Physical Review B*, 2006, **74**(17), P. 174431.
[57] Néel L. Magnetic properties of ferrites; ferrimagnetism and antiferromagnetism. *In Annales de physique*, 1948, 12(3), P. 137–198.
[58] Stoner E.C., Wohlfarth E.P. A mechanism of magnetic hysteresis in heterogeneous alloys. *Philosophical Transactions of the Royal Society of London. Series A*, 1948.
[59] Joshi G.P., Saxena N.S., Mangal R., Mishra A., Sharma T.P. Band gap determination of Ni-Zn ferrites. *Bulletin of Materials Science*, 2003, **26**(4), P. 387–389.
[60] Holinsworth B.S., Mazumdar D., Sims H., Sun Q.C., Yurtisigi M.K., Sarker S.K., Musfeldt J.L. Chemical tuning of the optical band gap in spinel ferrites: $CoFe_2O_4$ vs NiFe2O4. *Applied Physics Letters*, 2013, **103**(8), P. 082406.
[61] Nitika, Rana A., Kumar V. Tailoring the Structural, Magnetic, Mechanical, and Thermal Properties of $CoFe_2O_4$ by Varying Annealing Temperature for High-Density Storage Devices. *ECS Journal of Solid State Science and Technology*, 2021.
[62] Parishani M., Nadafan M., Dehghani Z., Malekfar R., Khorrami G.H.H. Optical and dielectric properties of NiFe2O4 nanoparticles under different synthesized temperature. *Results in physics*, 2017, **7**, P. 3619–3623.
[63] Yuliantika D., Taufiq A., Hidayat A., Hidayat N., Soontaranon S. Exploring Structural Properties of Cobalt Ferrite Nanoparticles from Natural Sand. *In IOP Conference Series: Materials Science and Engineering*, 2019, April, **515**(1), P. 012047.
[64] Pawar C.S., Gujar M.P., Mathe V.L. Optical properties of spin-deposited nanocrystalline Ni-Zn ferrite thin films processed by sol-gel. *Journal of Superconductivity and Novel Magnetism*, 2017, **30**(3), P. 615–625.